AGU PUBLICATIONS

JGR

Journal of Geophysical Research: Atmospheres

RESEARCH ARTICLE
10.1002/2016JD026202

Key Points:
- First study of sky waves from triggered lightning
- Effective ionospheric height increases with time for six sequential flashes during one-half hour before sunset
- Effective ionospheric height stays roughly constant for strokes within individual flashes

Correspondence to:
F. L. Carvalho,
fcarval1@ufl.edu

Citation:
Carvalho, F. L., M. A. Uman, D. M. Jordan, J. D. Hill, S. A. Cummer, D. A. Kotovsky, and R. C. Moore (2017), Triggered lightning sky waves, return stroke modeling, and ionosphere effective height, *J. Geophys. Res. Atmos.*, *122*, 3507–3527, doi:10.1002/2016JD026202.

Received 7 NOV 2016
Accepted 5 MAR 2017
Accepted article online 8 MAR 2017
Published online 24 MAR 2017

Triggered lightning sky waves, return stroke modeling, and ionosphere effective height

F. L. Carvalho[1], M. A. Uman[1], D. M. Jordan[1], J. D. Hill[2], S. A. Cummer[3], D. A. Kotovsky[1], and R. C. Moore[1]

[1]Department of Electrical and Computer Engineering, University of Florida, Gainesville, Florida, USA, [2]Scientific Lightning Solutions, LLC, Titusville, Florida, USA, [3]Department of Electrical and Computer Engineering, Duke University, Durham, North Carolina, USA

Abstract Ground waves and sky waves measured 209 km and 250 km south of six triggered lightning flashes containing 30 strokes that occurred in the half-hour before sunset on 27 August 2015 are presented and analyzed. We use a cross-correlation technique to find the ionospheric effective reflection height and compare our results to previous techniques that calculate effective height based on the time delay between ground wave and sky wave time domain features. From the first flash to the last flash there is, on average, a 1.6 km increase in effective ionospheric height, whereas no change in effective ionospheric height can be discerned along the individual strokes of a given flash. We show to what extent the triggered lightning radiation source can be described (using channel-base current, channel geometry, and channel luminosity versus time and height) and speculate that a well-characterized source could allow a more accurate determination of the electromagnetic fields radiated toward the ionosphere than has been done to date. We show that both channel geometry and the change in return stroke current amplitude and waveshape with channel height (inferred from measured channel luminosity versus height and time) determine the waveshape of the ground wave (and presumably the upward propagating wave that results in the sky wave) and that the waveshape of the ground wave does not appear to be related to the current versus time waveform measured at the channel base other than a roughly linear relationship between the two peak values.

1. Introduction

Characteristics of the *D* region of the ionosphere, the lower ionosphere between a height of about 60 km and 90 km, have been studied by a number of investigators from analyses of the ionospheric reflections—so-called sky waves—observed at ground level from the radio frequency electromagnetic radiation generated by natural cloud-to-ground lightning return strokes [e.g., *Kinzer*, 1974; *McDonald et al.*, 1979; *Cummer*, 2000; *Cheng and Cummer*, 2005; *Cheng et al.*, 2007; *Shao and Jacobson*, 2009; *Lay and Shao*, 2011a, 2011b; *Haddad et al.*, 2012; *Shao et al.*, 2013; *Lay et al.*, 2014; *Somu et al.*, 2015]. The primary disadvantage of using natural lightning strokes as the source of upward directed electromagnetic waves that interact with the ionosphere and result in downward directed sky waves is the lack of knowledge of the characteristics of the lightning source and hence of the upward radiated lightning signal. The upward propagating electric and magnetic fields prior to ionospheric reflection are difficult to measure, so generally only the component of the waveform that propagates across the Earth's surface, the so-called ground wave, is measured. The to-date-unexplored use of rocket-and-wire triggered lightning to generate ionosphere-probing sky waves involves a return stroke source that can be relatively well characterized, including measured current versus time at the base of the stroke channel, measured channel geometry above ground, and measured channel luminosity versus time and height, a proxy for channel current versus time and height [e.g., *Carvalho et al.*, 2015]. In the present paper we examine the measured source characteristics, ground waves, and sky waves that can be obtained by using triggered lightning data. In addition, we provide a sample data set demonstrating to what extent the triggered lightning radiation source can be characterized.

Previous studies of the ionosphere employing sky waves from natural lightning return strokes can be conveniently divided into two categories: (1) analyses that determine an effective reflecting height for the *D* region and the variation of that height with time, as well as the related features of the reflection, and (2) analyses that determine an electron density versus height for the *D* region and its variation with time.

Studies that fall in the first category compute an effective reflecting height by assuming specular reflection of all frequency components from the ionosphere and by measuring the time elapsed from a ground wave feature to its corresponding sky wave feature, such as (a) the beginning of the ground wave to the beginning of the sky wave [*Schonland et al.*, 1940; *Caton and Pierce*, 1952; *Kinzer*, 1974; *McDonald et al.*, 1979] and (b) the ground wave peak to the sky wave peak [*Lay and Shao*, 2011a, 2011b; *Somu et al.*, 2015; *Kolmašová et al.*, 2016]. In addition, lightning atmospherics have been used to probe the ionosphere by defining and analyzing parameters attributed to ionospheric variation such as the peak reflection ratio (R), defined as the magnitude of the sky wave peak divided by the magnitude of the ground wave peak [*Lay and Shao*, 2011a].

In the second category, electron density profiles versus height (h), modeled as the two parameter exponential given by *Wait and Spies* [1964]

$$N_e(h) = 1.43 \times 10^7 \cdot \exp(-0.15h') \cdot \exp[(\beta - 0.15)(h - h')]\mathrm{cm}^{-3} \quad (1)$$

where the constant h' controls the height of the profile and the constant β the sharpness of the ionospheric transition, have been calculated from measured sky waves by a number of groups [e.g., *Cummer et al.*, 1998; *McRae and Thomson*, 2000; *Cheng and Cummer*, 2005; *Han and Cummer*, 2010; *Lay et al.*, 2014]. Given a model for the electron density versus height, some groups have used it to compute the impulse response of different ionospheres, which is then convolved with the ground wave portion of atmospherics (a proxy for the upward propagating wave that is not measured), resulting in a modeled sky wave [e.g., *Hu and Cummer*, 2006; *Haddad et al.*, 2012; *Somu et al.*, 2015].

The ionosphere is a collection of electrons, ions, and neutral particles immersed in the Earth's magnetic field. The propagation of an electromagnetic wave in such a plasma is dispersive; that is, each frequency component comprising an original wideband time domain signal propagates differently. Frequencies above tens of MHz penetrate and escape the D region. Lower frequencies entering the bottom of the ionosphere at an angle from the normal are continuously refracted as they propagate toward higher electron density until they are "bent" downward toward the Earth and escape the ionosphere at the same angle they entered it (assuming a horizontally homogeneous plasma), although some of the lower frequencies can traverse the ionosphere as evidenced by the detection of whistlers above the D region [e.g., *Jacobson et al.*, 2016; *Lefeuvre et al.*, 2013]. In general, higher frequencies penetrate farther into the D region than lower frequencies. Clearly, there is no single reflection height and the apparent reflection height for a given frequency is a function of observation distance. Nevertheless, because sky waves often exhibit well-defined time domain waveforms with a well-defined starting point and other identifiable features, the time from some point on the ground wave, usually the beginning or the initial peak field, to some point on the sky wave, usually the beginning (or "slow/fast breakpoint" used in *McDonald et al.* [1979]), allows a determination of an absolute effective height for a reflection from an assumed reflecting surface.

In the present paper we use both the traditional technique (signal-feature identification) and time domain cross correlation to determine the time between individual sky waves from strokes in the same triggered flash and in successive triggered flashes, and hence to determine the effective ionospheric height versus time. We present measured ground waves and sky waves at 209 km and 250 km south of the triggered lightning source for six triggered lightning flashes containing 30 strokes that occurred between 23:24:26.5 and 23:53:23.4 UTC on 27 August 2015. During this time, the solar zenith angle at the triggering facility increased from approximately 84 to 90°, and the solar zenith angle at the measurement sites increased from approximately 85 to 92°, thus indicating that the probed ionospheric region was undergoing its sunset transition from daytime to nighttime conditions [e.g., *Ogawa and Shimazaki*, 1975; *Friedrich et al.*, 2001]. We note that the solar zenith angles were calculated by using the NOAA Solar Calculator, available at https://www.esrl.noaa.gov/gmd/grad/solcalc/azel.html. We show to what extent that the triggered-lightning return stroke source can be characterized and speculate that such a characterized radiation source could allow a more sophisticated determination of the electromagnetic fields radiated toward the ionosphere than has been done to date. We show that both channel geometry and the change in return stroke current amplitude and waveshape with channel height (inferred from measured channel luminosity versus height and time) determine the waveshape of the ground wave (and presumably the upward propagating wave) and that, in our data, the waveshape of the ground wave does not appear to be related to the current versus time waveform measured at the channel base other than a roughly linear relationship between the two peak

values. We infer from simple return stroke modeling that the electric field waveshape of the upward propagating wave prior to reflection from the ionosphere can be quite different from the ground wave.

2. Experiment

2.1. General

Lightning has been artificially initiated (triggered) from natural thunderstorms by using the rocket-and-wire technique [e.g., *Rakov and Uman*, 2003, Chapter 5] at the International Center for Lightning Research and Testing (ICLRT), located in north-central Florida, every summer since 1993. Typically, 20 to 30 flashes, each containing three or four return strokes, are triggered each summer. The return strokes in triggered lightning are similar, if not identical, to strokes after the first, so-called subsequent strokes, in natural cloud-to-ground lightning. On 27 August 2015, all six rockets launched in a one-half hour period triggered lightning flashes with multiple return strokes. The usual triggering rate for the rocket-and-wire technique is about 50 to 60%. The six triggered lightning flashes (University of Florida (UF) 15-38, 39, 40, 41, 42, and 43) produced five, six, three, five, six, and six return strokes, respectively. The identifier for each triggered flash presented in this paper begins with UF (University of Florida), followed by the last two digits of the year in which it was triggered, followed by the number of the rocket launch that year. For example, UF 15-38 refers to the flash triggered by the 38th rocket launched in the year 2015. The triggering took place between 19:25 and 19:55 local daylight saving time. There were no thunderstorms to disturb the ionosphere along the propagation path between the ICLRT and the two sky wave recording stations located 209 km and 250 km to the south, as evidenced in Figure 1 by the lack of any base reflectivity recorded by the National Weather Service Jacksonville (KJAX, point D in Figure 1) radar along a line between the three sites. Base reflectivity refers to the KJAX radar with elevation of 10 m, elevation angle of 0.5°, and beam width of 1°, which corresponds to an actual elevation between 600 and 1800 m at the ICLRT, about 70 km away. The storm from which the six flashes were triggered is just to the west of the point A in Figure 1.

In this paper, we evaluate the potential for using triggered lightning sky waves to determine ionospheric properties via electromagnetic and optical measurements of the six 27 August 2015 triggered lightning flashes. Presented measurements include (a) return stroke channel-base current, (b) channel luminosity versus time and height, (c) channel geometry via photography and the Lightning Mapping Array (LMA), (d) ground wave and sky wave electric fields measured at 209 km south of the ICLRT, and (e) ground wave and sky wave magnetic fields measured at 250 km south of the ICLRT. We describe these measurements next.

2.2. Current Measurement at Channel Base

Carvalho et al. [2014] describe the experimental setup for measuring the triggered-lightning channel-base current. Briefly, the current is measured on three scales (ranging from 40 A to 50 kA) as it flows through a noninductive 1 mΩ shunt resistor having a 45 ns 10–90% risetime to an input step current. The channel-base current is then digitized and transmitted through an optical fiber link to a LeCroy 44 Xi digital storage oscilloscope, which triggers whenever the current flowing through the channel-base current shunt resistor exceeds the threshold value of about 6 kA of either polarity [*Hill*, 2012, p. 84]. When triggered, this oscilloscope sends an output trigger pulse that is routed to the ICLRT master trigger box and a request is sent to the ICLRT GPS timing system to print the time (to the nearest 1 μs) to a text file. This time stamp is recorded and assigned to the corresponding return stroke of the current flash. Each return stroke with peak current greater than about 6 kA has its own GPS time stamp. If a return stroke has a current peak lower than about 6 kA, it is still recorded and time-tagged on a long time-base oscilloscope. The ICLRT channel-base current measurement is located at latitude 29°56′34.8″N and longitude 82°01′59.7″W.

2.3. Channel Luminosity Versus Height and Time

The photodiode array used to measure luminosity waveforms as a function of triggered lightning channel height and time consisted of 12 Thorlabs APD120A2 avalanche photodiode modules and 20 Thorlabs APD130A avalanche photodiode modules. Both types of photodiodes had the same −3 dB high-frequency cutoff, near 50 MHz (corresponding to about 10 ns 10–90% risetime to a step function of light). All 32 photodiodes were mounted on 0.6 m vertical structure located 293 m from the ICLRT field rocket launcher. As outlined in *Carvalho et al.* [2015], each photodiode was combined with an adjustable horizontal slit set at 0.51 mm located 140 mm in front of the photodide. The photodiodes were assembled on a Thorlabs

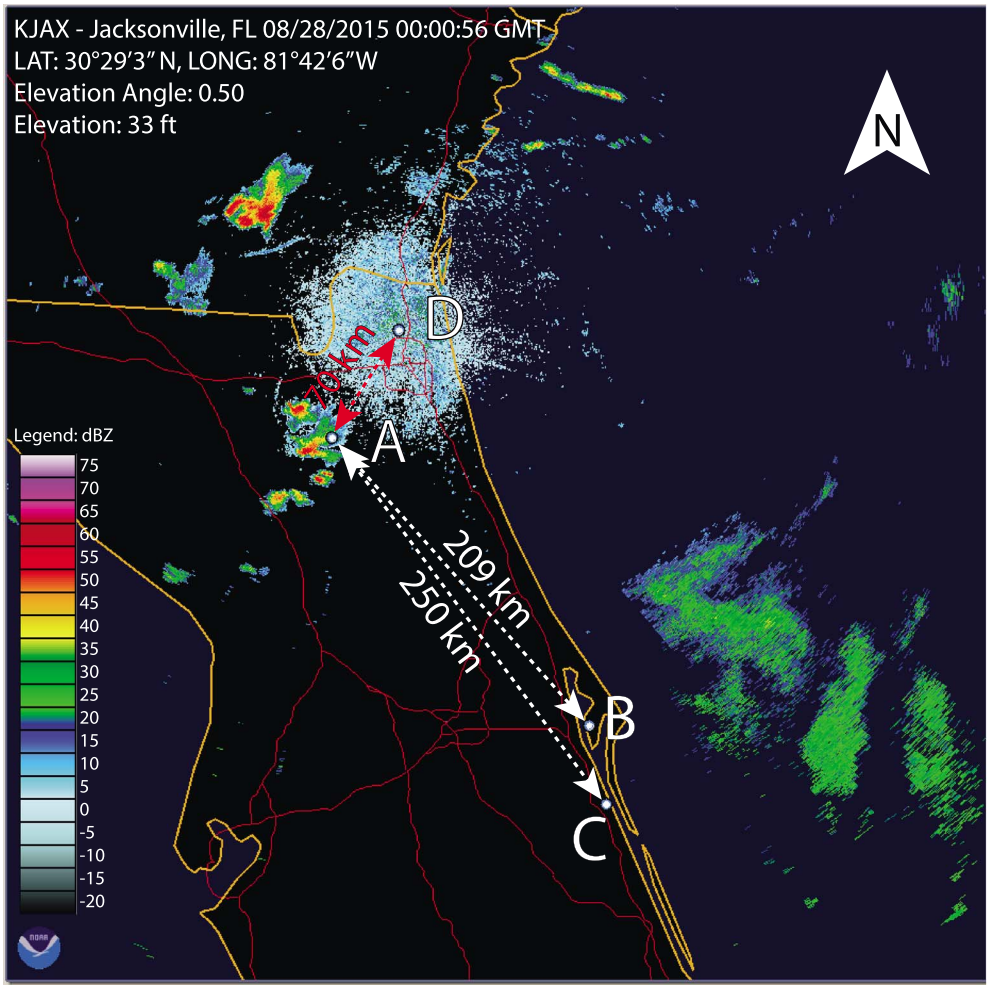

Figure 1. Base reflectivity (for 10.06 m elevation, 0.5° elevation angle, and 1° beam width, 70 km away) recorded by the National Weather Service Jacksonville (KJAX) radar on 28 August 2017 00:00:56 UTC (equivalent to 27 August 2017 20:00:56 local EDT time, approximately 3 min after the last rocket launch). Point A is the ICLRT, B is the UF E-field station (209 km south), C is the Duke *B*-field station (250 km south), and D is the KJAX radar (70 km northeast). There are no thunderstorms on the paths between A and B, nor between A and C (represented by the dashed lines), as evidenced by the low dBZ value in the radar image. The thunderstorm from which the six flashes were triggered is just west of point A.

lockable rotation platform RP01 with radial scale marked every 2°. The desired elevation angle above the horizon was calculated assuming a straight and vertical lightning channel for channel heights ranging from 4 m to 1000 m above the strike rod tip shown in Figure 1 of *Carvalho et al.* [2014]. A neutral density filter with an optical transmission of 10% was attached in front of the adjustable horizontal slits of photodiodes 1–15, 16, 19, 20, 23, 24, 26, 27, 29, and 30; no filter was attached to photodiodes 17, 18, 21, 22, 25, 28, 31, and 32. Increasing photodiode number generally indicates increasing elevation angle and viewing height.

The output of photodiodes 1 to 20 were digitized at 100 MHz in 10 ms segments and stored by using one four-channel 12 bit LeCroy HDO6054 having 500 MHz bandwidth and four four-channel 12 bit LeCroy HRO 64Zi oscilloscope having 400 MHz bandwidth. The outputs of photodiodes 21 to 32 were continuously digitized at either 10 MHz or 100 MHz for 500 ms and stored by using one 16-channel Yokogawa DL850 oscilloscope. The trigger generated when the channel-base current measurement exceeded the threshold value of about 6 kA was used to trigger the avalanche photodiode array. The pretrigger was set to 5 ms for all optical measurements.

2.4. Channel Geometry: Lightning Mapping Array and Photography

Pilkey et al. [2014] describes in detail the Lightning Mapping Array (LMA) system used during 27 August 2015 at the ICLRT. The LMA [e.g., *Rison et al.*, 1999; *Krehbiel et al.*, 2000; *Thomas et al.*, 2004; *Hill et al.*, 2012, 2013] is a continuously operating system used to locate VHF radiation sources associated with lightning discharges, generally related to the tips of propagating leaders. Figures 2–7 of *Pilkey* [2014] shows a diagram of a typical ICLRT LMA station. The ICLRT LMA system is composed of eight LMA stations. The LMA data were processed by using a time-of-arrival algorithm, allowing one to reconstruct temporal channel geometries from the detected and processed VHF sources emitted by lightning. The LMA system is primarily used to study the development and propagation of lightning above a few hundred meters altitude and inside the cloud, where direct photographs are not possible, and to infer the polarity of electric charge regions in the cloud [e.g., *Pilkey et al.*, 2014]. Illustrations of lightning channel geometry for natural and triggered lightning derived from the ICLRT LMA are found in *Hill et al.* [2013, Figure 4], *Dwyer and Uman* [2014, Figures 1.8 and 1.9], and *Pilkey et al.* [2014, Figure 4]. Location accuracy above a few hundred meters is on the order of 10 to 20 m [*Thomas et al.,* 2004].

In order to study the channel geometry below the cloud base, the ICLRT is equipped with a series of high-speed cameras, standard high-definition video cameras, and a network of still cameras. Here we present data from three of seven optical stations: Northeast Optical (NEO, located 430 m NE of the field rocket launcher), Southwest Optical (SWO, located 390 m southwest of the field rocket launcher), and Instrument Station-4 (IS-4, located 300 m west of the field rocket launcher). Each station was equipped with one Nikon digital single-lens reflex camera that had a 10 mm focal length and was programmed to take photographs with 6 s exposure time in order to capture the entirety of each triggered flash.

2.5. Electric Field Measurement 209 km South (UF Station)

The vertical component of the distant electric field was recorded at the UF station located 209 km south of the ICLRT on Merritt Island, FL (latitude 28°27′46.8″N, longitude 80°42′26.8″W), point B in Figure 1. The UF station is composed of an electric field antenna with a −3 dB upper frequency response of about 5 MHz and a decay time constant to a step function input of about 0.01 s. The distant electric field data were digitized at 10 MHz during 20 s segments and were recorded on a 12 bit LeCroy HDO6054 oscilloscope. Additionally, the IRIG-A time code output of the GPS timing system was connected to Channel 2 of the oscilloscope, providing UTC time synchronization of the recorded electric field waveforms to accuracy of about 1 μs.

The lightning electric field at 209 km was superimposed on an ambient 60 Hz power line noise. The 60 Hz interference was mitigated by computing and removing the approximately linear slope between the start and the end of the waveform, taken as 450 μs of electric field data containing a ground wave and its sky wave. In addition, an oscillatory signal at 1.3 MHz was present in the time domain electric field measurement. In order to optimally reproduce the original signal, the raw UF electric field data were processed by using a set of two linear Butterworth low-pass filters (LPF): one with a −3 dB frequency cutoff of 700 kHz (applied to the electric field measurement containing the peak radiation field, i.e., the ground wave) and another with a −3 dB frequency cutoff of 300 kHz (applied to the part of the signal containing the sky wave). These choices were made considering that ground wave features are sharper than those of sky waves, and therefore, ground wave signals require higher-frequency components to adequately reconstruct their features. Low-pass filtering to an upper frequency response of 700 kHz maintains all the observed salient features of the time domain ground wave that has had its high-frequency content attenuated in propagating over 209 km of Florida soil [e.g., *Uman et al.*, 1976; *Aoki et al.*, 2015; *Jiang et al.*, 2016]. In our data, the received ground wave 10–90% risetime exceeds 1 μs, similar to the experimental over-ground data of *Uman et al.* [1976] for natural subsequent strokes recorded at 200 km in Florida, whereas natural subsequent stroke ground waves propagating over salt water of relatively high conductivity, expected to produce significantly less propagation attenuation, exhibit submicrosecond risetimes [*Weidman and Krider*, 1980]. Similarly, all salient sky wave features are maintained after low-pass filtering the sky wave data to an upper frequency of 300 kHz.

2.6. Magnetic Field Measurement 250 km South (Duke Station)

The magnetic field measurement operated by Duke University is located 250 km south of the ICLRT on the campus of the Florida Institute of Technology, in Melbourne, FL (latitude 28°03′44.1″N, longitude 80°37′26.4″W), point C in Figure 1. Briefly, the dual ferrite-core magnetic loop antenna system

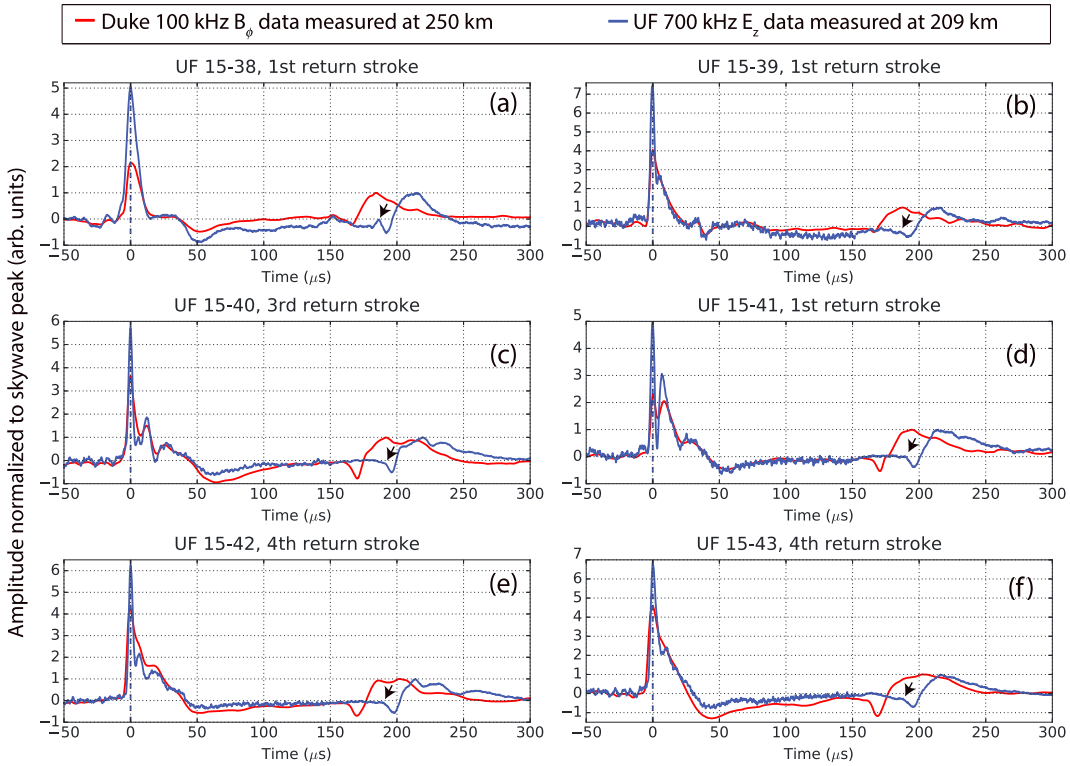

Figure 2. One example from each triggered lightning flash of 27 August 2015. In all plots, signals in blue represent the vertical electric field E_z measured at the UF station (209 km south of the striking point), point B in Figure 1. Signals in red represent the azimuthal magnetic field B_ϕ measured at the Duke station (250 km south), point C in Figure 1. All waveforms were amplitude normalized to the sky wave peak and shifted so that each ground wave peak aligns with an arbitrary time $t = 0$. The peak amplitudes of the channel-base current associated with each return stroke shown in Figures 2a–2f are 15.1 kA, 4.4 kA, 19.1 kA, 13.7 kA, 14.3 kA, and 20.5 kA, respectively. The black arrow indicates the slow breakpoint introduced by *McDonald et al.* [1979] and was determined subjectively by eye.

[*Cummer et al.*, 2011] measures both components of the azimuthal magnetic field at a sampling rate of 1 MHz with GPS-based timing. Data from this system presented here are postprocessed to have a relatively flat frequency response between 1 kHz and 100 kHz with a two-pole low-frequency roll-off below 1 kHz to suppress the ambient 60 Hz noise.

3. Data

Figure 2 shows the UF 209 km (point B in Figure 1) vertical electric field (blue curve) and the Duke 250 km (point C in Figure 1) azimuth magnetic field (red curve) for one large-current stroke from each of the six triggered flashes of 27 August 2015. The first, sharper peak of either curve in Figures 2a–2f is the ground wave portion of the overall waveform, and the second, broader peak is the sky wave, the start of which on the UF data being identified by a black arrow (also referred to as the "slow breakpoint" in *McDonald et al.* [1979]). The pairs of curves plotted in Figures 2a–2f were time aligned so their respective ground wave peaks are located at the arbitrary time $t = 0$ and were amplitude normalized to the peak *sky wave* maximum amplitude. The time difference between the ground wave and sky wave in the more distant magnetic field measurement (Duke B_ϕ, red curve) is smaller than the time difference between the same two waveforms of the closer electric field measurement (UF E_z, blue curve) because, at increasing distance from the source, the difference in the distances traveled by the ground wave and the sky wave becomes smaller. At relatively large distances, the ground wave path and the first-order sky wave path are so similar that the two merge into one complex waveform [*Schonland et al.*, 1940].

Figure 3 shows the sky wave vertical electric fields (Figure 3a) and sky wave azimuthal magnetic fields (Figure 3b) for each stroke of the six triggered flashes shown in Figure 2. The curves plotted in Figure 3a

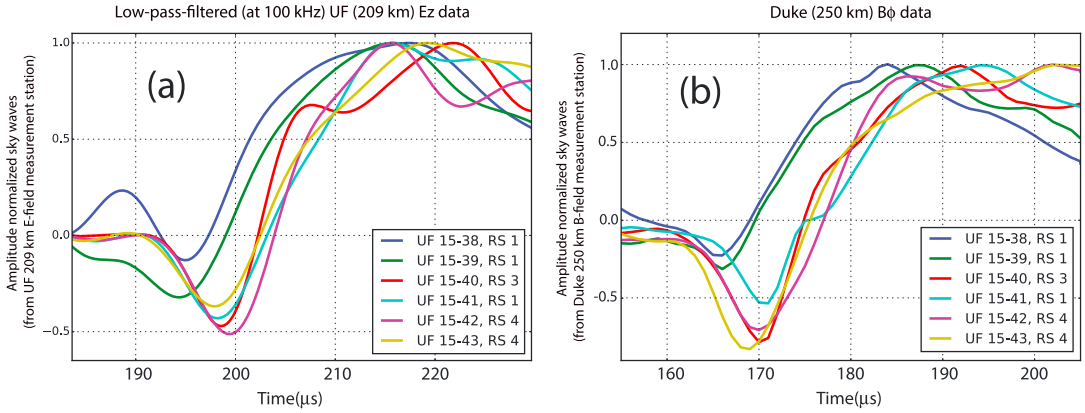

Figure 3. Sky wave from return stroke of each triggered flash shown in Figure 2 aligned in time to its respective 5% ground wave peak. Within the one-half hour between the first return stroke (UF 15-38, RS 1) and the last return stroke (UF 15-43, RS 4), the negative peak of each sky wave shifts in time, indicating an increase in the propagation path length within the six return strokes. (a) The time-aligned 209 km low-pass-filtered sky waves (UF's E_z). (b) The time-aligned 250 km sky waves from Duke's B_ϕ measurement.

are a zoomed version of the amplitude-normalized sky wave portion of the waveforms shown in Figure 2. All sky waves shown in Figure 3a are referred in time to the same point of the waveform: the 5% of peak value preceding the ground wave peak, our representation of the ground wave start time. Thus, a shift in time of a particular wave feature likely indicates a difference in the reflection characteristics from flash to flash. Within the one-half hour between the first return stroke (UF 15-38, RS 1) and the last return stroke (UF 15-43, RS 4), the negative sky wave peak (the so-called "fast breakpoint" of *McDonald et al.* [1979]), except for one stroke (UF 15-43, return stroke 4), appears later in time, indicating an increase in the propagation path length (that is, greater effective reflection height) within these six return strokes. The time elapsed from the first sky wave to each subsequent sky wave is different due to the fact that the interval between each triggered flash was different and that each return stroke radiated a distinct field waveshape. The corresponding azimuthal magnetic field data are shown in Figure 3b. A shift in time for sky wave features is also observed in the distant azimuthal magnetic field measurement, for ground waves aligned in time to their 5% amplitude level. Figure 3a shows the low-pass-filtered version of the original electric field measured at 209 km, and Figure 3b shows the original azimuthal magnetic field measured at 250 km.

Figure 4 shows the channel geometry of two triggered flashes, UF 15-38 and UF 15-41, the first with a relatively straight vertical channel geometry and the second with a channel having a horizontal section of well over 100 m length located a few hundred meters above ground. Figure 4a (Figure 4e) shows a photograph (6 s exposure) of UF 15-38 (UF 15-41) taken at the IS-4 station, located approximately 300 m west of the striking point. Figure 4b (Figure 4f) shows a photograph of UF 15-38 (UF 15-41) taken at the NEO station, located 430 m northeast of the striking point. Figure 4c (Figure 4g) shows a photograph of UF 15-38 (UF 15-41) taken at the SWO station, located 390 m southwest of the striking point. The angles from which each photograph was taken relative to the striking point are depicted by the black arrows in circles in Figures 4a–4c and 4e–4g. Figure 4d (Figure 4h) shows the amplitude normalized ground wave portion of the electric field signature of the sequential 5 (4) strokes measured at the UF 209 km station (point B in Figure 1) for flash UF 15-38 (UF 15-41). The ground wave in Figure 4d for UF 15-38, approximately vertical in the bottom 2 km, does not show a dip after the peak for the first two strokes of that flash, but does for all the following three strokes, whereas there is a pronounced dip for all strokes of UF 15-41, whose geometry included the long horizontal section at a height of a few hundred meters. For both flashes, the depth of the dip generally increases with increasing return stroke order. The same behavior is observed for all six triggered flashes studied here. For each return stroke in Figures 4d and 4h, we show the postprocessed electric field measured at UF (209 km) normalized to the ground wave peak and shifted in time so the reference time $t = 0$ is aligned to each ground wave peak. It is worth noting that we have observed many natural lightning first and subsequent stroke electric field waveforms with a dip, sometime below zero field, after the initial peak.

Figure 5 shows the VHF radiation sources associated with UF 15-38 and UF 15-41, from the ICLRT LMA system (see section 2.4). The two figures on the left (right) represent the channel geometry above a few

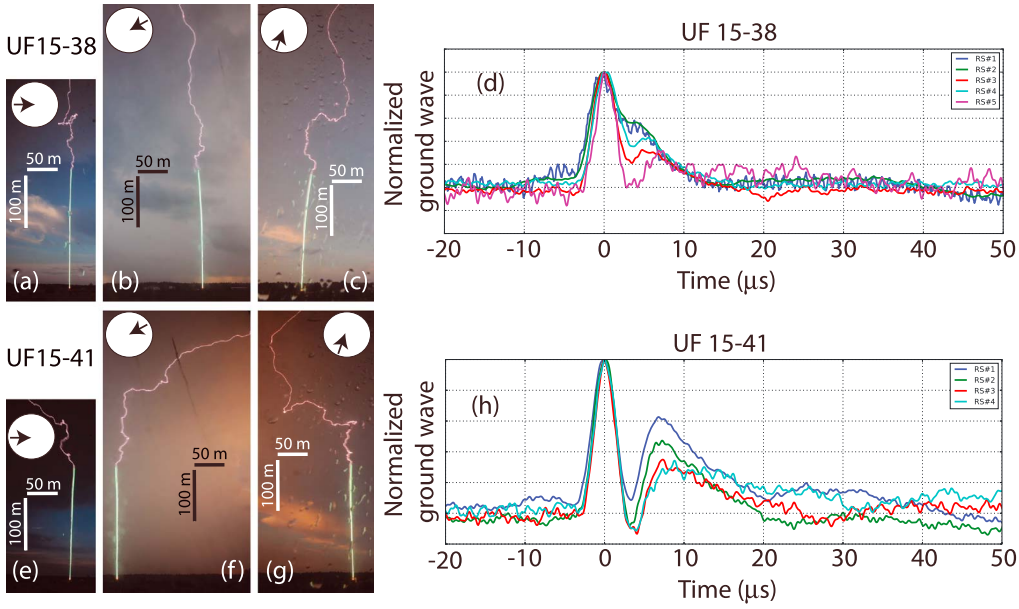

Figure 4. (a–h) Still photographs (6 s exposure) and distant ground wave electric field (from UF's 209 km station) for two triggered lightning flashes (UF 15-38 and UF 15-41). Figure 4a (Figure 4e) shows a photo of UF 15-38 (UF 15-41) taken 300 m west of the striking point. Figure 4b (Figure 4f) shows a photo of UF 15-38 (UF 15-41) taken 430 m northeast of the striking point. Figure 4c (Figure 4g) shows a photo of UF 15-38 (UF 15-41) taken 390 m southwest of the striking point. Figure 4d (Figure 4h) shows the amplitude normalized ground wave portion of the electric field signature measured at the UF station, located 209 km southeast from the striking point for the different return strokes in flash UF 15-38 (UF 15-41). Note that the ground wave dip after the initial peak increases with stroke order.

hundred meters in altitude looking in perpendicular directions, south-north and west-east, for event UF 15-38 (UF 15-41). The LMA figures on the left (right) are cut off at 4.5 km (5.5 km) altitude and include sources for all leaders and return strokes and *M* components for UF 15-38 (UF 15-41). Clearly, there are major deviations from a vertical channel in the 2 to 4 km altitude range.

The evidence from LMA sources and photography is that all return strokes and the other processes in each flash followed the same path in the bottom few kilometers above ground, the channel height from which

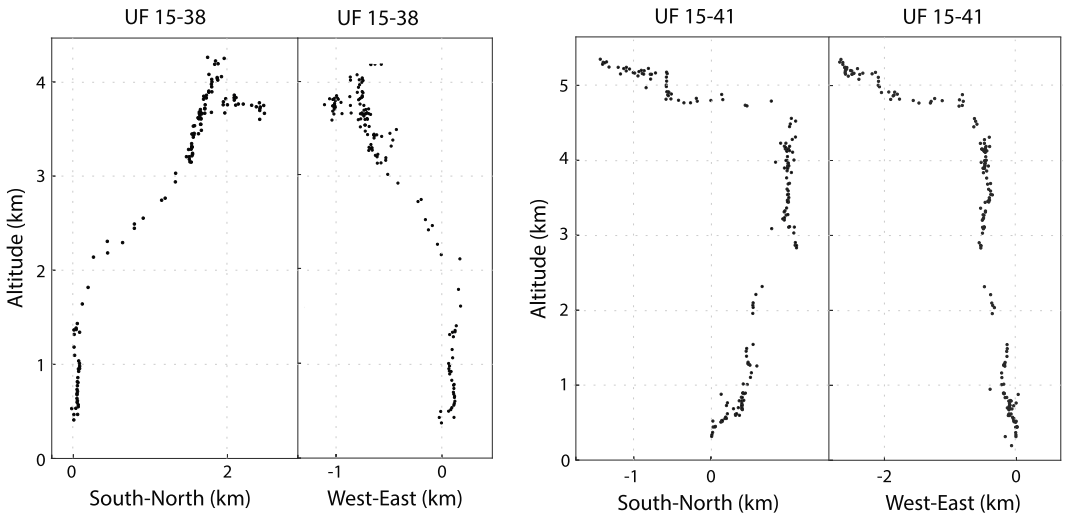

Figure 5. Lightning channel geometry from VHF LMA radiation sources associated with lightning discharges for events (left) UF 15-38 and (right) UF 15-41.

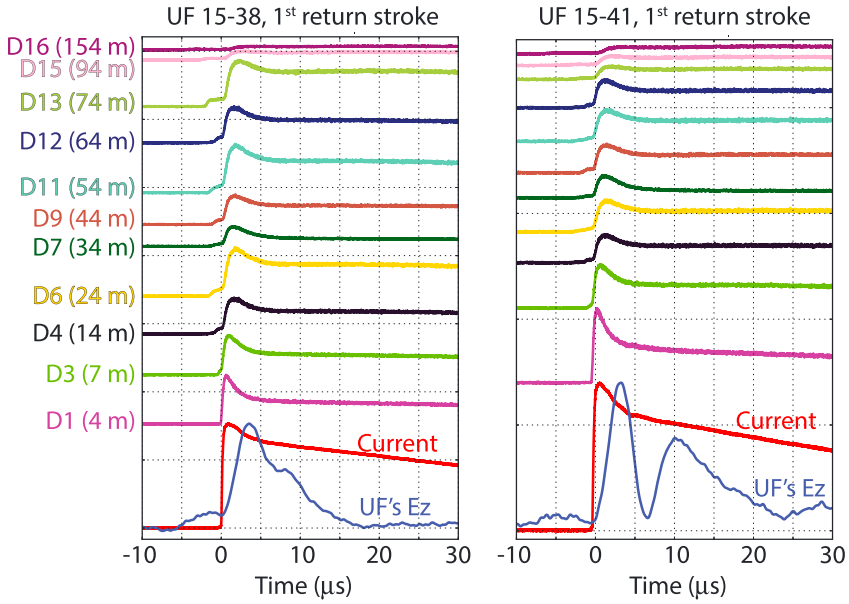

Figure 6. Two examples of triggered-lightning channel-base current (red) plotted with distant ground wave electric field from the 209 km UF station (blue) and luminosity profiles versus time and height. (left) UF 15-38, RS 1 (15.4 kA of channel-base current peak amplitude). (right) UF 15-41, RS 1 (13.7 kA of channel-base current peak amplitude). In both examples, and for the bottom 150 m of the triggered lightning channel, the amplitude of the luminosity waveforms decreases with increasing height, while luminosity risetimes increase with increasing height. For all return strokes analyzed in this article, the channel-base current has 10–90% risetimes 1 order of magnitude less than that of the distant electric field at 209 km due to propagation distortion of the ground wave. The half-peak width for the channel-base current is significantly greater than that of the 209 km E_z.

the ground wave of about 50 μs duration likely emanated. The large dip following the ground wave peak in UF 15-41 (Figure 4h) occurs about 10 μs from the beginning of the ground wave, probably a few microseconds less if waveform spreading due to propagation over a nonperfectly conducting ground is taken into account (see section 4) and does not appear in the current measured at ground. Thus, for a typical return stroke speed of c/3, the return stroke current front is probably near 1 km when the dip occurs, or lower if the speed is faster. The radiated field emanates from current in all sections of the channel below the front and is apparently influenced by channel geometry for UF 15-41.

Figure 6 shows two examples of triggered-lightning stroke channel-base current plotted with the UF (209 km) electric field and source-stroke luminosity profile versus time and height. UF 15-38, RS 1 is plotted on the left (15.4 kA channel-base current peak amplitude) and UF 15-41, RS 1 is plotted on the right (13.7 kA channel-base current peak amplitude). In both plots, the red and blue curves represent the amplitude normalized channel-base current and distant ground wave electric field measured at the UF's 209 km station, respectively. We present the data in this form so as to emphasize that the distant propagation-distorted electric field (see section 2.5) rises to its peak about an order of magnitude slower than the current and decreases from its peak about an order of magnitude faster than the current (see Table 1 for detailed risetime and half-width value measurements as well as the peak current and electric field data from each stroke). The measured electric field does not appear to be correlated with features of the current waveform except that the peak electric field and the peak current are correlated, as shown in Appendix A and Figure A1. Above the two amplitude-normalized current and UF electric field curves, we present the raw data recorded by 12 out of 32 simultaneously triggered avalanche photodiodes, indicating how the luminosity progressed, given a current traveling upward along the triggered-lightning return-stroke channel, as a function of channel height and time. The luminosity data presented in Figure 6 were taken in the bottom 150 m and hence along the wire section of the triggered lightning channel, and thus, small remnants of copper along the return stroke channels are likely to exist [e.g., *Walker*, 2015], even though the copper wire exploded hundreds of milliseconds before the first stroke. The measured luminosity waveforms along and in the air above the wire

Journal of Geophysical Research: Atmospheres

10.1002/2016JD026202

Table 1. Summary of 27 August 2015 Events

Local Time (hh-mm-ss)	Event Name	Return Stroke Number	Channel-Base Peak Current (kA)	Ground Wave Peak (Arb. Units)	Channel-Base Current 10–90% Risetime (s)	Ground Wave 10–90% Risetime (s)	Channel-Base Current 5%-Peak Risetime (s)	Ground Wave 5%-Peak Risetime (s)	Channel-Base Current Half-Peak Width (s)	Ground Wave Half-Peak Width (s)
19-24-26.522908895	UF15-38	1	15.1	0.58	2.88E − 07	2.00E − 06	7.90E − 07	3.00E − 06	4.18E − 05	6.30E − 06
19-24-26.579535265	UF15-38	2	21.5	0.80	2.20E − 07	2.40E − 06	4.16E − 07	3.60E − 06	3.20E − 05	6.80E − 06
19-24-26.69109798	UF15-38	3	15.4	0.41	2.14E − 07	1.60E − 06	4.68E − 07	2.80E − 06	7.19E − 06	3.10E − 06
19-24-26.73455787	UF15-38	4	12.6	0.36	1.84E − 07	1.70E − 06	4.16E − 07	2.30E − 06	1.14E − 05	3.60E − 06
19-24-26.764446	UF15-38	5	6.1	0.08	1.10E − 07	1.99E − 06	2.02E − 07	2.42E − 06	1.97E − 06	2.90E − 06
19-32-06.583436840	UF15-39	1	4.4	0.40	1.03E − 05	1.90E − 06	1.80E − 05	3.10E − 06	5.39E − 05	3.40E − 06
19-32-06.58655284	UF15-39	2	10.2	0.17	4.96E − 07	1.60E − 06	1.36E − 06	2.10E − 06	3.12E − 05	3.10E − 06
19-32-06.633136315	UF15-39	3	5.1	0.26	7.75E − 07	1.70E − 06	1.43E − 06	2.40E − 06	2.12E − 05	3.00E − 06
19-32-06.671758785	UF15-39	5	8.6	0.24	1.72E − 07	1.60E − 06	3.78E − 07	2.60E − 06	7.61E − 06	2.90E − 06
19-41-20.7469716	UF15-40	2	14.0	0.56	3.60E − 07	1.90E − 06	7.15E − 07	2.80E − 06	3.88E − 05	3.20E − 06
19-41-20.76746508	UF15-40	3	19.1	0.72	2.94E − 07	2.10E − 06	1.05E − 06	3.20E − 06	4.74E − 05	3.30E − 06
19-43-57.29844679	UF15-41	1	13.7	0.43	3.36E − 07	1.70E − 06	9.44E − 07	2.70E − 06	3.47E − 05	3.11E − 06
19-43-57.373669615	UF15-41	2	11.1	0.35	4.48E − 07	2.00E − 06	9.86E − 07	2.80E − 06	2.64E − 05	3.07E − 06
19-43-57.40511691	UF15-41	3	11.0	0.30	2.28E − 07	1.70E − 06	4.54E − 07	2.30E − 06	9.59E − 06	2.70E − 06
19-43-57.555913445	UF15-41	4	11.4	0.26	1.76E − 07	1.80E − 06	4.68E − 07	2.50E − 06	4.11E − 06	3.00E − 06
19-43-57.57506654	UF15-41	5	5.2	0.08	3.38E − 07	1.50E − 06	5.28E − 07	2.00E − 06	9.16E − 06	2.30E − 06
19-47-42.712899355	UF15-42	1	7.9	0.24	3.28E − 07	1.60E − 06	7.82E − 07	2.70E − 06	2.02E − 05	3.10E − 06
19-47-42.8627664	UF15-42	3	13.0	0.38	2.14E − 07	1.70E − 06	4.22E − 07	2.40E − 06	1.81E − 05	3.40E − 06
19-47-43.05818559	UF15-42	4	22.5	0.74	2.58E − 07	2.10E − 06	4.90E − 07	3.00E − 06	1.94E − 05	3.70E − 06
19-47-43.33809311	UF15-42	5	14.3	0.31	5.02E − 07	1.90E − 06	1.08E − 06	2.60E − 06	4.28E − 06	3.10E − 06
19-47-43.36631259	UF15-42	6	16.5	0.50	1.96E − 07	1.80E − 06	4.26E − 07	2.60E − 06	1.17E − 05	3.40E − 06
19-53-22.706011205	UF15-43	1	14.8	0.59	2.38E − 07	2.50E − 06	4.20E − 07	5.70E − 06	4.34E − 05	5.70E − 06
19-53-22.934697575	UF15-43	2	14.2	0.47	2.54E − 07	2.10E − 06	4.34E − 07	3.10E − 06	3.81E − 05	5.10E − 06
19-53-23.157666725	UF15-43	3	17.6	0.49	2.80E − 07	2.00E − 06	5.18E − 07	2.80E − 06	1.06E − 05	3.90E − 06
19-53-23.293418545	UF15-43	4	20.5	0.68	2.22E − 07	2.30E − 06	4.22E − 07	3.20E − 06	2.46E − 05	5.30E − 06
19-53-23.38995781	UF15-43	5	7.7	0.15	1.96E − 07	1.50E − 06	3.96E − 07	2.00E − 06	3.59E − 06	2.70E − 06
Average (μ)[a]			12.8	0.41	2.93E − 07	1.87E − 06	6.40E − 07	2.78E − 06	2.07E − 05	3.67E − 06
Standard deviation (σ)[a]			5.1	0.20	1.41E − 07	2.74E − 07	3.26E − 07	7.22E − 07	1.42E − 05	1.19E − 06

[a]Excludes the first return stroke of UF 15-39 because of its unusual current risetime.

have similar waveshape characteristics, although we do not show any data above the wire here. In general, the amplitude of the luminosity waveforms decreases with increasing height, while luminosity risetimes increase with increasing height. Apparently, the return stroke current behaves in a closely related manner [e.g., *Carvalho et al.*, 2014, 2015]. Recent analyses indicate that the return stroke current upward speed is up to 30% faster than the speed of the luminosity, but the waveshapes may not be significantly different [*Carvalho et al.*, 2014, 2015]. Measured luminosity amplitude is in part related to the angle of the channel with respect to the vertical, imaged on the horizontal slit (see section 2.3).

4. Analysis

4.1. Measurements on Triggered Lightning Current and Distant Electric Field

A summary of the salient features of the UF channel-base current (measured at point A in Figure 1) and 209 km electric field waveforms (measured at point B in Figure 1) is given in Table 1. For each of the 26 ground waves without a large noise component, we give the peak amplitude, the 10-to-90% risetime, the 5%-to-peak risetime, and the half-width time for both ICLRT channel-base current and the postprocessed distant vertical electric field measured at the UF (209 km) station.

4.2. Change in Ionospheric Height With Time

In order to study the variations with time of the ionospheric effective reflection height, we select the waveform portion containing the sky waves of pairs of different return strokes in the same and different flashes and cross correlate both signals to compute the lag time between the two different sky waves. Each waveform is assumed to have a starting point which is at the 5% amplitude level preceding ground wave peak, a much better approximation to the time of arrival of the ground wave than the peak value, given the lengthening of the ground wave risetime from submicrosecond to microsecond due to propagation over a poorly conducting Earth (see section 2.5).

If we assume a simple geometry composed of a horizontal ground and a horizontal ionosphere (as depicted in Appendix B and Figure B1), ignore the effects of the Earth's curvature (because our remote sensing devices are located at 209 km and 250 km, relatively close to the source at which distance the Earth's curvature has no substantial impact on the results), and assume specular wave reflection, as done in many previous studies [e.g., *Kinzer*, 1974; *McDonald et al.*, 1979; *Haddad et al.*, 2012; *Somu et al.*, 2015], then the distance traveled by the sky wave of the first triggered stroke to a remote sensing station is

$$D_1 = 2\sqrt{h_1^2 + \left(\frac{r}{2}\right)^2} \tag{2}$$

where h_1 is the effective reflection height and r is the distance between the ICLRT triggered lightning channel base and the UF electric field station (209 km) or the Duke magnetic field station (250 km). Similarly, the distance traveled by the sky wave of a different return stroke is

$$D_2 = 2\sqrt{h_2^2 + \left(\frac{r}{2}\right)^2} \tag{3}$$

where h_2 is the effective reflection height at that later time and r is the same horizontal distance. Assuming a temporal variation in the virtual reflection height, it follows that

$$h_2 = h_1 + \Delta h \tag{4}$$

where Δh is the variation in the effective reflection height of return stroke pairs. Δh can be directly computed from the lag time between the two waveforms, Δt_{lag}, which we will do by two techniques: cross correlation and waveform-feature identification. In this section we apply the cross-correlation technique. For ground wave propagation speed assumed equal to c between the ICLRT and UF electric field station, this simple relationship is true

$$\frac{(D_2 - D_1)}{c} = \Delta t_{lag} \tag{5}$$

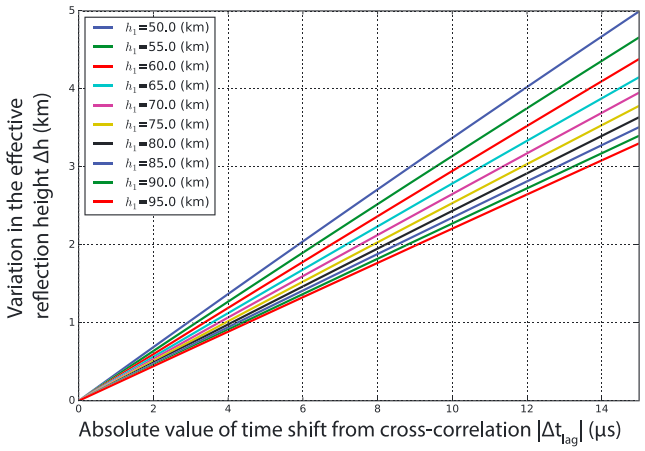

Figure 7. Variation in the effective reflection height as a function of the time shift from cross correlation ($|\Delta t_{lag}|$) for different values of h_1. For $|\Delta t_{lag}| = 5$ μs, the change in Δh due to a wide range of h_1 (varying from 50 km to 90 km) is about 600 m and only around 130 m for h_1 varying from 75 km to 90 km.

To verify that the ground wave speed is approximately equal to c, we measured the time delay between the 6 kA trigger point on the return stroke current and the 5% of the peak value of the electric field at 209 km for all 26 return strokes presented in Table 1. The mean of the measured ground wave speed was 2.91×10^8 m/s, with 0.59×10^8 m/s of standard deviation, made with a timing uncertainty on the order of 1 μs, for a propagation time of about 700 μs, resulting in a relatively small error in any calculations done in this paper, all calculations in this paper being made assuming $c = 2.99 \times 10^8$ m/s.

Equation (5) can be solved for Δh by combining equations (2)–(4) given above:

$$\Delta h = h_1 - \frac{1}{2}\sqrt{4 \cdot h_1^2 + \left(c \cdot \Delta t_{lag}\right)^2 + \left(4 \cdot c \cdot \Delta t_{lag}\right) \cdot \sqrt{h_1^2 + \left(\frac{r}{2}\right)^2}} \quad (6)$$

Figure 7 shows a plot of Δh as a function of Δt_{lag} (equation (6), above) for different values of h_1 to show that the results obtained for the change in height (Δh) from one sky wave to the next are not much influenced by the value of the absolute height (h_1). From Figure 7, it is clear that for relatively small values for Δt_{lag}, on the order of a few microseconds, the change of the ionospheric effective reflection height is less than 1 km. For example, for $|\Delta t_{lag}| = 5$ μs, Δh is about 600 m for a wide range of h_1 (varying from 50 km to 90 km) and only about 130 m for h_1 varying from 75 km to 90 km (the commonly reported range of effective reflection heights). A negative value for Δt_{lag} means that the sky wave being compared to the "reference sky wave" (see next paragraph) must be shifted in time to the left in order to achieve the maximum cross-correlation value. In other words, a negative value for Δt_{lag} corresponds to an increase in Δh.

In Figure 8a, we plot from equation (6), assuming $h_1 = 80$ km [*Smith et al.*, 2004, Figure 6], the change in the effective reflection height (Δh) that results from the cross correlation within two data sets: UF E_z (sky waves low-pass-filtered to 300 kHz), in blue, and Duke B_ϕ (100 kHz measurement bandwidth). Figure 8a shows the increase in the effective reflection height (Δh), referred to the first return stroke of UF 15-38, computed from the cross-correlation result (lag time, Δt_{lag}) using equation (6) applied to the two data sets mentioned above. The plot in Figure 8a indicates an upward trend within the one half-hour before sunset containing all the six triggered flashes for all four data sets. In order to account for the errors associated with computing the lag time from cross correlation, we follow the method presented in *Tonry and Davis* [1979] and fit a Gaussian pulse with the form $g(t) = \frac{1}{\sigma\sqrt{2\pi}} \exp - \frac{(t-\mu)^2}{2\sigma^2}$ to the cross-correlation pulse. In $g(t)$, σ is the standard deviation, μ is the expected value, and t is the time. If the Gaussian pulse $g(t)$ fits well the cross-correlation output, Δt_{lag}, along with its error analysis, can be easily extracted from the fit parameter μ of $g(t)$. This is indeed the case, and as seen in Table 2, the Gaussian function $g(t)$ is a sound approximation to the cross-correlation output, evidenced by the high values for goodness of fit (R^2) and the low values for rms fit error (rmse). Finally, because the Gaussian function $g(t)$ accurately represents the cross-correlation output, the fit parameter μ (expected value) and its 95% confidence bounds are equivalent to the Δt_{lag} shown in equation (6) and used to compute Δh . The vertical lines plotted in Figure 8a represent the errors associated with computing Δh. The source of the errors represented in Figure 8a by the vertical lines are twofold: (1) the ± 130 m associated with the Δh span resulting from selecting h_1 varying from 70 to 90 km and (2) the Δh calculated from the 95% confidence bounds of the fit parameter μ.

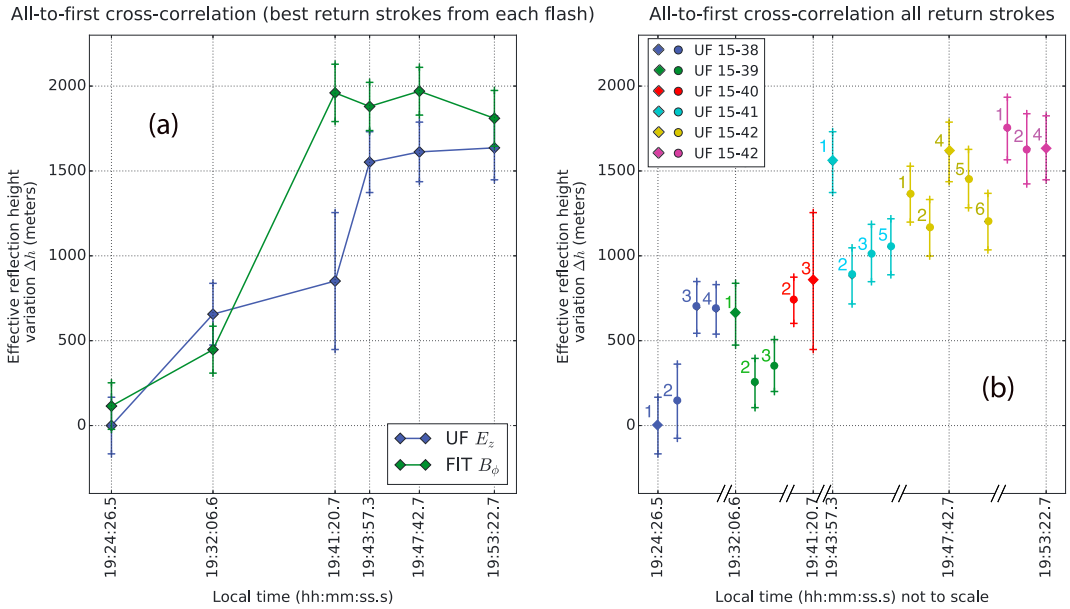

Figure 8. (a and b) "All-to-first" cross-correlation results from ground wave 5% peak amplitude. Figure 8a shows the all-to-first cross-correlation results for one large-current return stroke of each triggered flash (same as those in Figure 2) in two data sets: Duke's B_ϕ and UF's E_z (low-passed-filtered at 300 kHz). Figure 8b shows the all-to-first cross-correlation results for all 21 return strokes with good sky wave signal-to-noise ratio recorded by the UF's E_z station (and low-passed-filtered at 300 kHz). The diamonds represent the selected large-current return stroke of each flash (same as the blue diamonds in Figure 8a), the circles represent all the other return strokes, and the numbers represent the return stroke order. All return strokes of each triggered flash are plotted in the same color. The vertical error bars in both figures were computed from the 95% confidence bounds of the expected value, μ, found from fitting a Gaussian pulse to the cross-correlation output. The x axis of Figure 8b is nonlinear so as to emphasize the variations in the effective reflection height (Δh) on two time scales: within each flash (milliseconds), and between different flashes (minutes). There is an overall upward trend within the one half-hour time window from the first to the last return stroke but no coherent change for the strokes within each of the six flashes.

Table 2. Cross-Correlation Results for 21 Pairs of Sky Waves[a]

Data 1	Data 2	x_{corr} Gaussian Fit (R^2)	rmse	Δt_lag (s)	Δt_lag 95% Bounds (s)	Δh (m)	Δh Error (m)
UF 15-38, 1	**UF 15-38, 1**	**0.964**	**10.19**	**0.00E + 00**	**1.50E − 07**	**0.00**	**37**
UF 15-38, 1	UF 15-38, 2	0.922	0.45	−5.84E − 07	3.60E − 07	143.65	89
UF 15-38, 1	UF 15-38, 3	0.999	0.72	−2.84E − 06	9.11E − 08	696.07	22
UF 15-38, 1	UF 15-38, 4	1.000	0.60	−2.79E − 06	6.41E − 08	684.59	16
UF 15-38, 1	**UF 15-39, 1**	**0.962**	**11.79**	**−2.68E − 06**	**2.11E − 07**	**656.27**	**52**
UF 15-38, 1	UF 15-39, 2	0.998	1.28	−1.02E − 06	6.00E − 08	250.61	15
UF 15-38, 1	UF 15-39, 3	0.997	1.38	−1.44E − 06	9.49E − 08	353.66	23
UF 15-38, 1	UF 15-40, 2	1.000	0.07	−3.01E − 06	2.27E − 08	738.14	6
UF 15-38, 1	**UF 15-40,3**	**0.994**	**3.17**	**−3.47E − 06**	**1.12E − 06**	**851.39**	**273**
UF 15-38, 1	**UF 15-41, 1**	**0.997**	**2.54**	**−6.35E − 06**	**2.02E − 07**	**1552.00**	**49**
UF 15-38, 1	UF 15-41, 2	0.992	0.97	−3.60E − 06	1.45E − 07	881.72	35
UF 15-38, 1	UF 15-41, 3	0.998	2.85	−4.15E − 06	7.15E − 08	1016.60	17
UF 15-38, 1	UF 15-41, 5	0.999	0.92	−4.30E − 06	1.58E − 07	1053.20	39
UF 15-38, 1	UF 15-42, 1	0.998	1.53	−5.57E − 06	1.42E − 07	1362.60	35
UF 15-38, 1	UF 15-42, 3	0.997	2.27	−4.76E − 06	1.49E − 07	1165.30	36
UF 15-38, 1	**UF 15-42, 4**	**0.996**	**2.69**	**−6.60E − 06**	**1.88E − 07**	**1612.30**	**46**
UF 15-38, 1	UF 15-42, 5	0.998	0.14	−5.95E − 06	1.74E − 07	1455.10	42
UF 15-38, 1	UF 15-42, 6	0.997	2.17	−4.91E − 06	1.50E − 07	1201.50	37
UF 15-38, 1	UF 15-43, 1	0.997	2.35	−7.16E − 06	2.24E − 07	1750.10	54
UF 15-38, 1	UF 15-43, 2	0.999	1.98	−6.67E − 06	3.16E − 07	1630.40	77
UF 15-38, 1	**UF 15-43, 4**	**0.998**	**1.95**	**−6.70E − 06**	**2.40E − 07**	**1636.20**	**58**
Average (μ)		0.991	2.48	−4.03E − 06	2.06E − 07	985	50
Standard Deviation (σ)		0.019	2.98	2.16E − 06	2.25E − 07	528	55

[a]Rows with bold text represent the return strokes considered in Figure 2.

Table 3. Absolute Reflecting Height Using the Two Versions of the Traditional Time Domain Method (Slow Breakpoint and Fast Breakpoint)

			Duke's *B* Field		UF's E Field (LPF Ground Wave at 700 kHz, Sky Wave at 300 kHz)		Duke's *B* Field		UF's E Field (LPF Ground Wave at 700 kHz, Sky Wave at 300 kHz)	
Local Time (hh-mm-ss)	Event Name	Return Stroke Number	Elapsed Time From 5% Ground Wave Amplitude Level to Slow Breakpoint (s)	Absolute Reflecting Height (km)	Elapsed Time From 5% Ground Wave Amplitude Level to Slow Breakpoint (s)	Absolute Reflecting Height (km)	Elapsed Time From 5% Ground Wave Amplitude Level to Fast Breakpoint (s)	Absolute Reflecting Height (km)	Elapsed Time From 5% Ground Wave Amplitude Level to Fast Breakpoint (s)	Absolute Reflecting Height (km)
19-24-26.522908895	UF15-38	1	1.57E − 04	80.23	1.90E − 04	81.98	1.72E − 04	84.20	1.97E − 04	83.89
19-32-06.583436840	UF15-39	1	1.63E − 04	81.77	1.91E − 04	82.22	1.71E − 04	83.93	1.98E − 04	83.95
19-41-20.76746508	UF15-40	3	1.64E − 04	82.04	1.94E − 04	82.99	1.77E − 04	85.53	2.00E − 04	84.48
19-43-57.29844679	UF15-41	1	1.65E − 04	82.31	1.91E − 04	82.42	1.75E − 04	85.00	2.00E − 04	84.51
19-47-43.05818559	UF15-42	4	1.65E − 04	82.31	1.92E − 04	82.49	1.75E − 04	85.00	2.01E − 04	84.73
19-53-23.293418545	UF15-43	4	1.66E − 04	82.58	1.90E − 04	82.17	1.75E − 04	85.00	2.02E − 04	84.99

Each diamond of Figure 8a represents the effective reflection height variation between different pairs of return strokes. For example, the first diamond, located at time 19:24:26.5 EDT, equals approximately zero for both data sets because it was computed from the Δt_{lag} found by cross correlating the sky wave of the first return stroke of UF 15-38 with itself (i.e., $\Delta t_{lag} = 0$). Similarly, the second diamond, located at time 19:32:06.6 EDT, represents the selected return stroke of UF 15-39 cross correlated with that reference return stroke (UF 15-38, RS 1); the third diamond, located at time 19:41:20.7 EDT, is the selected return stroke of UF 15-40 cross correlated with that same reference return stroke (UF 15-38, RS 1); and so forth. As a result, each diamond represents the Δh computed from the cross-correlation result (lag time, Δt_{lag}) relative to the reference return stroke (UF 15-38, RS 1) for each of the four data sets. The cross correlation was performed between one selected return stroke of each flash to the same reference return stroke (UF 15-38, RS 1) for each of the two data sets. The selected return strokes are shown in Figures 2a–2f.

Figure 8b is an expansion of Figure 8a, which shows the variation in the effective reflection height (Δh) for all UF sky waves not having a large noise component in the portion of the electric field signal containing the sky wave. We note that Table 1 presents five more return strokes than Figure 8b because the former contains information about ground waves (greater signal-to-noise ratio (SNR)) and the latter about sky waves (lower SNR). The results plotted in Figure 8b were computed from 21 pairs of UF (209 km) E_z sky waves low-pass-filtered to 300 kHz. The diamonds in Figure 8b are the same as the blue diamonds of Figure 8a and represent the results of the cross-correlation operation between the selected large-current return strokes of each flash (depicted in Figures 2a–2f) and the reference return stroke (UF 15-38, RS 1). The circles represent the results from cross correlating all other return strokes to the same reference return stroke (UF 15-38, RS 1). The numbers in Figure 8b represent the return stroke order within each flash. Each flash is plotted in a different color. The *x* axis of Figure 8b is nonlinear so as to emphasize the variations in the effective reflection height (Δh) on two time scales: within each flash (milliseconds), and within different flashes (minutes). Our results show that for different return strokes within the same flash, there is no coherent trend for Δh. For example, the Δh values calculated for different return strokes of UF 15-38 (blue) tend to increase with increasing return stroke order, whereas the Δh values computed for different return strokes of UF 15-43 (magenta) tend to decrease with increasing return stroke order. Thus, the return stroke order does not seem to affect Δh in a coherent way, which implies that within measurement error, strokes after a given stroke in a flash do not systematically penetrate deeper or less deep into the *D* region of the ionosphere (see section 5). Additionally, in the results plotted in Figure 8b, $|\Delta h|$ seems not to be directly correlated with the return stroke peak current. For example, the sky wave of UF 15-43, RS 4 has

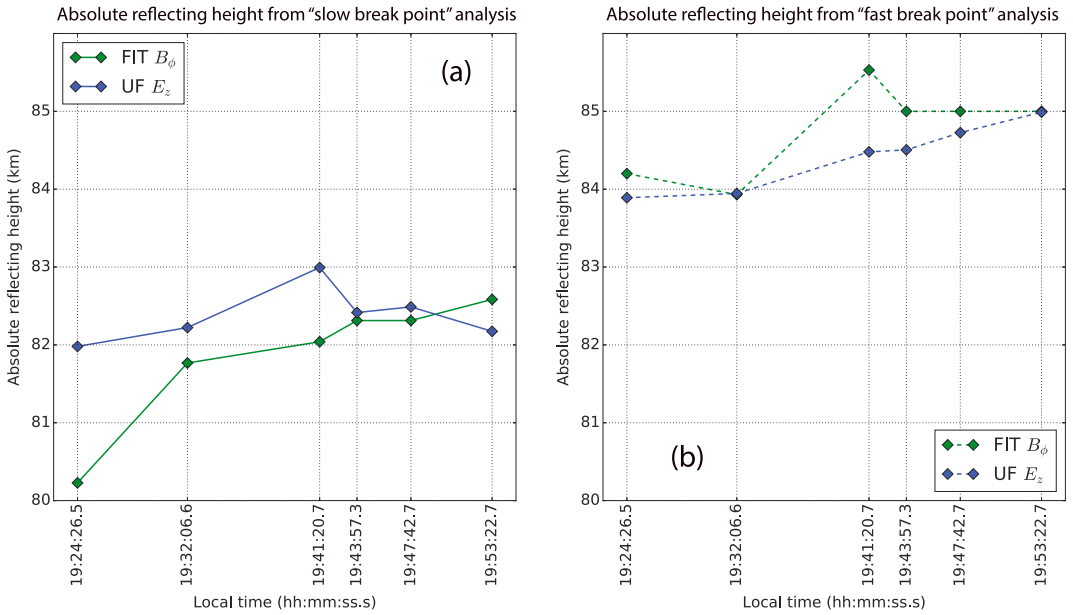

Figure 9. (a and b) Absolute reflecting height computed by using the traditional method of *McDonald et al.* [1979]. Figure 9a shows the absolute reflecting height calculated by using equation (7) and the time elapsed from the 5% ground wave peak to the sky wave slow breakpoint. Figure 9b shows the absolute reflecting height calculated by using equation (7) and the time elapsed from the 5% ground wave peak to the sky wave fast breakpoint.

a lower value for Δh than the sky wave of UF 15-43, RS 1, though the former has a larger peak current than the latter. Conversely, the sky wave of UF 15-41, RS 1 has the highest value of Δh within that flash even though it also has the largest peak current of the flash.

Although the process of ionospheric reflection is not actually specular [e.g., *Westcott*, 1962a, 1962b], our cross-correlation analysis indicates that the overall path traveled by the sky wave generally increased within the 30 min period ranging from the time elapsed from the first to the last triggered flashes (as seen in Figures 8a and 8b). The final flash was triggered 3 min prior to sunset (19:57 EDT, 23:57 UTC). Presumably, the increase in effective ionospheric height is because solar-radiated ionization decreases as the sun sets. See further comments with references in section 5.

Table 2 shows the cross-correlation results used to plot Figures 8a and 8b.

4.3. Absolute Ionospheric Effective Reflecting Height Versus Time

In this section we adopt the signal-feature identification, the approach of *McDonald et al.* [1979], to determine ionosphere height. We estimated an absolute reflecting height for the broadband vertical electric field and azimuthal magnetic field by tracking the time elapsed from the beginning of the ground wave (5% of ground wave peak) to the slow breakpoint (black arrows in Figures 2a–2f, determined by eye—see Figure 3 of *McDonald et al.* [1979] for a detailed definition) or to the fast breakpoint (easily identifiable negative peaks in Figures 2a–2f) and used those time delays to estimate the reflecting height based on simple geometry (horizontal ground and horizontal ionosphere, assuming specular reflection; Figure B1). The results from this calculation are shown in Table 3, where h is found from the time delay between the 5% of the ground wave peak to the slow breakpoint (or fast breakpoint), $\Delta\tau$, according to the equation below:

$$h = \frac{\sqrt{c\Delta\tau(2r_1 + c\Delta\tau)}}{2} \tag{7}$$

where c is the speed of light (see comments after equation (5)) and r_1 is the horizontal distance between source and recording station; detailed in Figure B1.

Figure 9a (Figure 9b) shows the effective reflecting height of the same data sets of Figure 8a calculated from the time delay between the 5% ground wave peak level and the sky wave slow breakpoint (fast breakpoint) for one large-current return stroke within each triggered flash (same strokes plotted in Figure 2). The results

obtained by using the traditional technique [*Kinzer*, 1974; *McDonald et al.*, 1979] show differences in the virtual reflection height for the data measured at 209 km and at 250 km. As expected, the heights found from the fast breakpoint (Figure 9b) are higher than those from the slow breakpoint (Figure 9a), because the former occurs later in time than the latter. From the differential analysis of the UF data, Δh increases and reaches its maximum around 19:53:22 EDT local time. The results from the traditional slow breakpoint technique, however, are highly dependent on the point chosen by eye to be the beginning of the sky wave, the results from the fast breakpoint less so. Our cross-correlation technique for finding Δh is independent of the slow/fast breakpoints and does not require one to choose the start of the sky wave; thus, the technique described in section 4.2 is more robust because the lag time between two curves is found analytically from a signal-processing tool: cross correlation. Although our technique does not give an absolute height directly, we showed in Figure 7 that the error introduced to the absolute height by selecting the initial value of h_1 is small. In Figure 9a the absolute reflecting height from the Duke 250 km data, representing incidence on the ionosphere at a shallower angle from the vertical than the UF 209 km data, is lower than the UF data, as might be expected from theory [e.g., *Westcott*, 1962b].

5. Discussion

Haddad et al. [2012] suggested that the electromagnetic field of the first return stroke of a natural lightning flash caused a descent of the ionospheric *D* layer because the observed difference in arrival times of the ground wave and its interpreted sky wave was considerably smaller for subsequent return strokes than for first strokes. While we cannot adequately test their first stroke versus subsequent strokes suggestion with triggered lightning (triggered lightning does not exhibit the more complex behavior of natural first return strokes following an initial stepped leader), we can say that their speculation that "there may be a cumulative effect of multiple strokes in lowering the ionospheric reflection height" is not evident, based on our results plotted in Figure 8b. In our data set, and using the cross-correlation technique, on average, from one flash to the next, $|\Delta t_{\mathrm{lag}}| = 1.09$ μs (with 0.91 μs standard deviation) corresponding to a $|\Delta h| = 268$ m, with no apparent upward nor downward trend within the same flash. In our data, there is not sufficient evidence to conclude that the reflecting layer systematically lowers from one return stroke to the next.

The data used in *Haddad et al.* [2012] were recorded under primarily daytime conditions, while the data presented in this paper were recorded a half-hour to minutes before sunset. We reasonably conjecture that the transition from day to night in our data may have an effect on the apparent increase of the reflecting layer, as previously observed [e.g., *Schonland et al.*, 1940; *Smith et al.*, 2004; *Han and Cummer*, 2010; *Lay and Shao*, 2011a, 2011b; *Lay et al.*, 2014].

The dips in the ground waves recorded by the UF's 209 km electric field station for UF 15-38 and UF 15-41 shown in Figures 4d and 4h increase in magnitude with return stroke order, for UF 15-38 after the first two return strokes, and for UF 15-41 for all return strokes. The increase of dip magnitude with stroke order is a general feature of all six triggered flashes. Since the channel geometry was observed to be constant for all return strokes in each flash (see Figures 4a–4c, 4e–4g, and 5), only a change in the way the return stroke current travels along the triggered lightning channel (e.g., magnitude, waveshape, front speed versus time and height) would create differences in the distant ground wave electric radiation field. We first examine the potential causes for a prominent dip in the electric field waveform in general and then consider the potential causes of the stroke-to-stroke changes in the dip. Note that *Willett et al.* [2008] have examined the role of channel shape in producing the observed electric ground wave field but not specifically the origin of the initial dip that we consider here.

Consider the case of a three-section channel: straight and vertical from 0 to a height *H*, then straight and horizontal of length *x* from the top of *H*, then vertical from the far end of *x* to infinity, as shown in Figure 10a. To examine zeroth-order effects, we assume a pure transmission line model for the return stroke current, that is a current that propagates along the channel from ground at constant speed *v* and maintains a constant waveshape, the distant radiation electric field at *r*. According to the transmission line theory of *Uman et al.* [1975] the distant radiation field for this situation is

$$E_z(r,t) = \left(\frac{v}{2\pi\epsilon_0 c^2 r}\right) \cdot \left[I\left(t-\frac{r}{c}\right) - I\left(t-\frac{H}{v}-\frac{r}{c}\right) + I\left(t-\frac{H}{v}-\frac{r}{c}-\frac{x}{v}\right)\right] \tag{8}$$

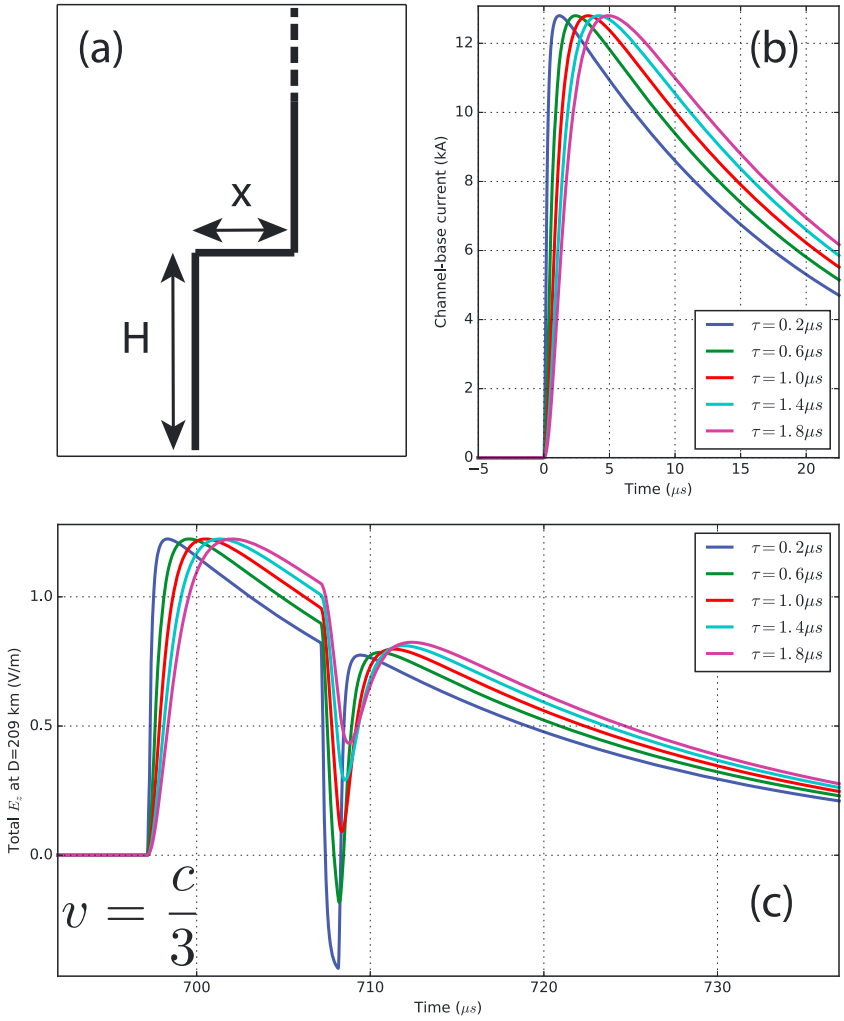

Figure 10. (a–c) Modeled ground wave with dip after peak radiation. Figure 10a shows the channel geometry used in the model, where $H = 1$ km and $x = 100$ m. Figure 10b shows the different inputs to the model: channel-base currents with different risetimes. Figure 10c shows the distant vertical electric field calculated from the channel geometry model described in the text. The model predicts increasing dip magnitude in the distant radiation electric field for decreasing current risetimes.

where I is the channel-base current, ϵ_0 is the permittivity of free space, c is the speed of light, v is the return stroke front speed, r is the horizontal distance between channel-base and measuring station (209 km), H is the height of the first vertical channel segment, and x is the length of the horizontal channel section.

The first term on the right of equation (8) represents the vertical radiation electric field as the current wave is launched upward from ground level, the second term the vertical electric field from the termination of the current's upward progression at H, and the last term is the vertical field from the current wave propagating upward from the distant end of x. There is no vertical field at far distance r from the horizontal current segment between H and x. The first term indicates a vertical field in the shape of the current which starts to exhibit a significant dip at $t = H/v$ and has that dip terminated at $t = H/v + |x - H|/v$. In a channel with horizontal sections like UF 15-38 and UF 15-41, the start and stop dip times, H/v and $H/v + |x - H|/v$, respectively, are on the microsecond time scale if the vertical and horizontal distances involved are on the order of 100 m. To the extent that the current wave on the three-section channel changes characteristics as it propagates along the channel, the overall waveform will be modified from that in equation (8). For example, if the current attenuates to zero before it reaches the height H, only some version of the first term on the right in equation (8) will be present, and there will be no dip in the distant electric field waveform. Even if the

total channel is vertical, it is possible, however, to find a current waveshape versus time and height that results in a small dip in the distant electric field [e.g., *Shao et al.*, 2012].

One explanation for the observed increasing dip magnitude with stroke order would be to hypothesize that early stroke currents were strongly attenuated with height prior to reaching horizontal or tortuous regions, while later stroke currents were less attenuated because of the channel conditioning due to prior strokes. In this scenario, the later strokes would better approximate the pure transmission line model.

A second interpretation to the increasing dip magnitude with stroke order is illustrated in Figure 10c, where the channel-base current risetime of Figure 10b was varied between 0.2 μs and 1.8 μs. The geometry used to get the results shown in Figure 10c is shown in Figure 10a for $H = 1$ km and $x = 100$ m, with $v = c/3$. If the horizontal channel segment length connecting the two vertical channel segments is kept the same, for faster current risetimes (i.e., risetimes less than $x/v = 1$ μs), the negative dip of the field radiated by the first vertical segment reaches its peak faster and before the field radiated by the second vertical segment is turned on. If the current rises slowly, the negative peak of the radiated field from the first vertical segment reaches its negative peak after the current for the second vertical segment is turned on, thus decreasing the magnitude of the ground wave dip. There is some evidence in our data that current risetime decreases with stroke order (see Table 1).

Although it is beyond the scope of this paper and will be the subject of a future paper, we speculate that from the present ground-based current, channel geometry, and channel luminosity versus time and height a consistent model for the ground wave fields could be constructed for the six triggered flashes (30 strokes, potentially). Given an adequate representation of the ground wave field, the model could then be used to compute the upward propagating wave that interacts with the ionosphere. Note that in the simple model described above, the mechanisms that produce the electric field dips in the ground wave may produce upward propagating maxima given the fact that the radiated field is strongest perpendicular to a current element. Detailed computer modeling taking account of the measured data and the conducting Earth is required in order to calculate the upward propagating wave.

6. Summary

In this paper, we have presented and analyzed electric and magnetic field ground waves and sky waves measured 209 km and 250 km south of six triggered lightning flashes containing 30 strokes that occurred in the half-hour before sunset on 27 August 2015. Sky waves recorded at 250 km arrive a few tens of microseconds earlier relative to the corresponding ground wave peaks than those measured at 209 km.

We showed that return strokes from sequential triggered lightning flashes that were aligned in time to the same ground wave feature (e.g., the 5% amplitude level preceding ground wave peak) exhibit a discernible time increase (on the order of 5 to 10 μs) in the sky wave start time ("slow/fast breakpoint"), implying an increase with time in the effective ionospheric height (on the order of 1 to 2 km) from which the sky waves reflect.

Using a cross-correlation technique we showed that from the first flash to the last flash there was, on average, a 1.6 km increase in effective ionospheric height. In our data, however, there was not sufficient evidence to conclude that the effective reflecting layer systematically changed from one return stroke to the next within a flash. The traditional technique for calculating the ionospheric effective reflecting height applied to the slow breakpoint and to the fast breakpoint leads to differences in the estimated reflecting height on the order of a few kilometers. In contrast, the cross-correlation technique, with relatively small uncertainties on the order of a few hundred meters, does not depend on subjectively selected points in the time domain waveform.

We provided two examples of return stroke luminosity profiles versus height and time showing that, in general, the luminosity peak amplitude decreases with increasing channel height, while the luminosity risetime increases with increasing height, in accordance with previous studies.

We showed that in our data, the waveshape of the distant return stroke ground wave does not appear to be related to the current versus time waveform measured at the channel base other than a roughly linear relationship between the two peak values. In addition, we presented measurements indicating that the distant

ground wave electric field rises to peak an order of magnitude slower and decays an order of magnitude faster than the measured channel-base current. The former effect is due to ground wave propagation over a nonperfectly conducting Earth. The latter effect is attributed to the attenuation and distortion of the return stroke current as it propagates up the leader channel.

We presented two examples of measured triggered lightning channel geometry to an altitude of a few kilometers by using both photography and VHF radiation source location to demonstrate that the lightning channel is far from straight and vertical. Triggered lightning channel geometry was shown to be likely a causative factor in producing dips in the ground wave field following the initial peak. Our data exhibited an increase in the depth of the dip magnitude with stroke order. We employed a simple return stroke transmission line model for a channel containing both a straight vertical and an elevated and horizontal section to predict an increase in dip magnitude with stroke order, related to either the postulated current attenuation with height as a function of stroke order or to the decrease in current risetime as a function of stroke order observed for some flashes.

We measured the time delay between the 6 kA trigger amplitude on the return stroke current and the 5% of the peak value of the electric field at 209 km for 26 return strokes and showed that the ground wave speed, measured in this way, is, on average, 2.91×10^8 m/s, with 0.59×10^8 m/s of standard deviation, very close to the speed of light $c = 2.99 \times 10^8$ m/s. The uncertainty in this measurement is on the order of 1 μs, for a propagation time of about 700 μs.

Finally, we speculated that from the geometry and luminosity data presented in this paper, a consistent return stroke model reproducing the ground wave fields could be constructed for all six triggered flashes (30 strokes, potentially). That model could then be used to compute the upward propagating waves that directly interact with the ionosphere to produce the distant-measured sky waves. The upward propagating wave is expected to have a different waveshape from the ground wave, at least in the cases where the ground wave exhibits a large dip after peak attributable to channel geometry, a not-uncommon feature in both triggered and natural lightning.

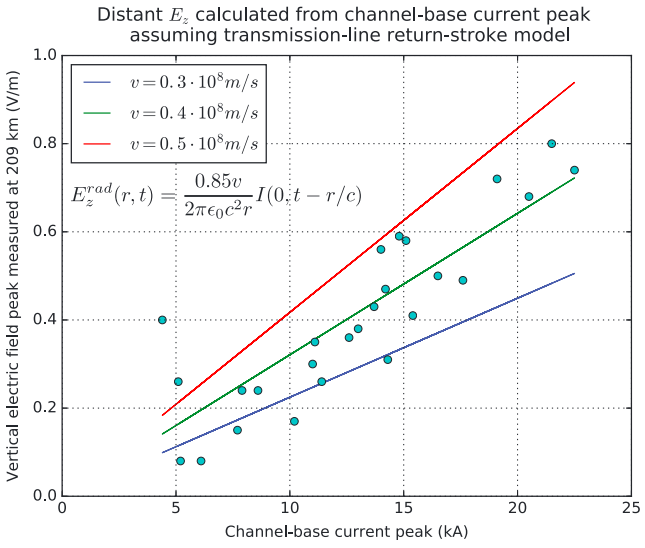

Figure A1. Distant vertical electric field versus channel-base current peak. The dots represent the data measured at UF 209 km station (shown in columns 4 and 5 of Table 1). The green (red, blue) line represents the vertical electric field peak calculated from channel-base current peak by using the transmission-line return stroke model when the return stroke front speed, assumed constant, equals 0.4×10^8 m/s (0.5×10^8 m/s, 0.3×10^8 m/s) and the radiation electric field peak has been attenuated to 0.85 of its original value. The green line represents the best fit to the scattered data plotted in cyan and has a coefficient of determination $R^2 = 0.75$.

Appendix A

We show here that a roughly linear relationship exists between the measured ground wave peak and the measured channel-base current peak. Figure A1 shows a plot of the measured data from columns 4 and 5 of Table 1, evidencing a strong positive correlation coefficient ($p = 0.87$) between ground wave peak and channel-base current peak. The circles in Figure A1 represent the data for the ground wave peak and the channel-base current peak for the 26 return strokes presented in Table 1. We use the transmission-line return stroke model to theoretically calibrate the vertical electric field. In order to do so, we find the best linear fit (green curve) passing through the origin for the scattered data of Figure A1 and solve for the return stroke current speed (v) by using a version of the transmission-line

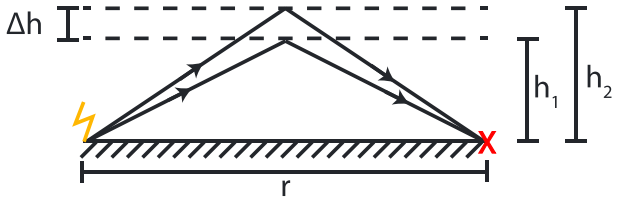

Figure B1. Geometry used in the cross-correlation analysis (used to derive equation (6)) for a specular reflection off a horizontally uniform ionosphere.

equation below. The green line represents the best fit for the scattered data plotted in cyan and has a coefficient of determination $R^2 = 0.75$ and value $v = 0.4 \times 10^8$ m/s. The red and blue curves are plotted so as to demonstrate the tight range of the return stroke front speed, v (from 0.3×10^8 m/s to 0.5×10^8 m/s).

$$E_Z^{\mathrm{rad}}(\mathrm{r},\mathrm{t}) = 0.85\frac{v}{2\pi\epsilon_0 c^2 r}\mathrm{I}\left(0, t - \frac{r}{c}\right) \tag{A1}$$

Equation (A1) is the first term on the right of equation (8) for a straight vertical channel except that the multiplicative 0.85 factor was included here so as to account for the average ground wave peak attenuation due to 209 km propagation over a nonperfectly conducting ground. Note that the factor of 0.85 is an estimate based on material in the literature (see last paragraph of section 2.5), and, in general, the sharper the unattenuated (close range) peak, the greater the attenuation of the peak with distance. We also note that there is an inherent trade-off between the ground wave attenuation factor and the return stroke propagation speed and the speed range, as evidenced in equation (A1). The speeds reported here may well be higher if the attenuation coefficient is lower than 0.85. A plot of measured peak electric field at 45 km from triggered lightning versus measured peak channel-base current, very similar to our Figure A1, is found in *Mallick et al.* [2012, Figure 4]. The peak electric field values measured by our system and presented in Table 1, when normalized to 100 km (0.86 V/m, on average), agree reasonably well with previous initial peak amplitudes of subsequent return strokes [*Rakov and Uman*, 1990; *Lin et al.*, 1979; *Cooray and Lundquist*, 1982].

Appendix B

Figure B1 shows the geometry used in the cross-correlation analysis (used to derive equation (6)) for a specular reflection off a horizontally uniform ionosphere.

Acknowledgments

This work was supported by DARPA/US Air Force through contract FA8650-15-C-7535 and by Tau Beta Pi through the 2016-2017 fellowship 37 (Williams). The data for this paper are available upon request from F.L. Carvalho (e-mail: fcarval1@ufl.edu). Because creating triggered lightning is a team effort, the authors wish to thank all involved, in alphabetical order: J.A. Caicedo, B.M. Hare, and R.A. Wilkes.

References

Aoki, M., Y. Baba, and V. A. Rakov (2015), FDTD simulation of LEMP propagation over lossy ground: Influence of distance, ground conductivity, and source parameters, *J. Geophys. Res. Atmos.*, *120*, 8043–8051, doi:10.1002/2015JD023245.

Carvalho, F. L., D. M. Jordan, M. A. Uman, T. Ngin, W. R. Gamerota, and J. T. Pilkey (2014), Simultaneously measured lightning return stroke channel-base current and luminosity, *Geophys. Res. Lett.*, *41*, 7799–7805, doi:10.1002/2014GL062190.

Carvalho, F. L., M. A. Uman, D. M. Jordan, and T. Ngin (2015), Lightning current and luminosity at and above channel bottom for return strokes and M-components, *J. Geophys. Res. Atmos.*, *120*, 10,645–10,663, doi:10.1002/2015JD023814.

Caton, P. G. F., and E. T. Pierce (1952), The waveforms of atmospherics, *Philos. Mag.*, *43*, 393–409.

Cheng, Z., and S. A. Cummer (2005), Broadband VLF measurements of lightning-induced ionospheric perturbations, *Geophys. Res. Lett.*, *32*, L08804, doi:10.1029/2004GL022187.

Cheng, Z., S. A. Cummer, H.-T. Su, and R.-R. Hsu (2007), Broadband very low frequency measurement of *D* region ionospheric perturbations caused by lightning electromagnetic pulses, *J. Geophys. Res.*, *112*, A06318, doi:10.1029/2006JA011840.

Cooray, V., and S. Lundquist (1982), On the characteristics of some radiation fields from lightning and their possible origin in positive ground flashes, *J. Geophys. Res.*, *87*(C13), 11,203–11,214, doi:10.1029/JC087iC13p11203.

Cummer, S. A. (2000), Modeling electromagnetic propagation in the Earth–ionosphere waveguide, *IEEE Trans. Antennas Propag.*, *38*(9), 1420–1429, doi:10.1109/8.898776.

Cummer, S. A., U. S. Inan, and T. F. Bell (1998), Ionospheric *D* region remote sensing using VLF radio atmospherics, *Radio Sci.*, *33*(6), 1781–1792, doi:10.1029/98RS02381.

Cummer, S. A., G. Lu, M. S. Briggs, V. Connaughton, S. Xiong, G. J. Fishman, and J. R. Dwyer (2011), The lightning-TGF relationship on microsecond timescales, *Geophys. Res. Lett.*, *38*, L14810, doi:10.1029/2011GL048099.

Dwyer, J. R., and M. A. Uman (2014), The physics of lightning, *Phys. Rep.*, *534*(30), 147–241, doi:10.1016/j.physrep.2013.09.004.

Friedrich, M., R. Pilgram, and K. M. Torkar (2001), A novel concept for empirical D-region modeling, *Adv. Space Res.*, *27*(1), 5–12.

Haddad, M. A., V. A. Rakov, and S. A. Cummer (2012), New measurements of lightning electric fields in Florida: Waveform characteristics, interaction with the ionosphere, and peak current estimates, *J. Geophys. Res.*, *117*, D10101, doi:10.1029/2011JD017196.

Han, F., and S. A. Cummer (2010), Midlatitude daytime *D* region ionosphere variations measured from radio atmospherics, *J. Geophys. Res.*, *115*, A10314, doi:10.1029/2010JA015715.

Hill, J. D. (2012), The mechanisms of lightning leader propagation and ground attachment, PhD dissertation, Univ. of Florida, Gainesville.

Hill, J. D., J. Pilkey, M. A. Uman, D. M. Jordan, W. Rison, and P. R. Krehbiel (2012), Geometrical and electrical characteristics of the initial stage in Florida triggered lightning, *Geophys. Res. Lett.*, *39*, L09807, doi:10.1029/2012GL051932.

Hill, J. D., J. Pilkey, M. A. Uman, W. Rison, P. R. Krehbiel, M. I. Biggerstaff, P. Hyland, and R. Blakeslee (2013), Correlated lightning mapping array and radar observations of the initial stages of three sequentially triggered Florida lightning discharges, *J. Geophys. Res. Atmos.*, *118*, 8460–8481, doi:10.1002/jgrd.50660.

Hu, W., and S. A. Cummer (2006), An FDTD model for low and high altitude lightning-generated EM fields, *IEEE Trans. Antennas Propag.*, *54*(5), 1513–1522, doi:10.1109/TAP.2006.874336.

Jacobson, A. R., R. H. Holzworth, R. Pfaff, and R. Heelis (2016), Automated identification of discrete, lightning- generated, multiple-dispersed whistler waves in C/NOFS-VEFI very low frequency observations, *Radio Sci.*, *51*, 1547–1569, doi:10.1002/2016RS005989.

Jiang, Z. D., B. H. Zhou, S. Qiu, and L. H. Shi (2016), Propagation effects on the electric field time derivatives generated by the stepped leaders and return strokes in CG flashes, *IEEE Trans. Electromagn. Compat.*, *58*(1), 125–134, doi:10.1109/TEMC.2015.2487359.

Kinzer, G. D. (1974), Cloud-to-ground lightning versus radar reflectivity in Oklahoma thunderstorms, *J. Atmos. Sci.*, *31*, 787–799.

Kolmašová, I., O. Santolík, T. Farges, S. A. Cummer, R. Lán, and L. Uhlíř (2016), Subionospheric propagation and peak currents of preliminary breakdown pulses before negative cloud-to-ground lightning discharges, *Geophys. Res. Lett.*, *43*, 1382–1391, doi:10.1002/2015GL067364.

Krehbiel, P. R., R. J. Thomas, W. Rison, T. Hamlin, J. Harlin, and M. Davis (2000), Lightning mapping observations in central Oklahoma, *Eos. Trans. AGU*, *81*(3), 21–25, doi:10.1029/00EO00014.

Lay, E. H., and X.-M. Shao (2011a), High temporal and spatial-resolution detection of D-layer fluctuations by using time-domain lightning waveforms, *J. Geophys. Res.*, *116*, A01317, doi:10.1029/2010JA016018.

Lay, E. H., and X.-M. Shao (2011b), Multi-station probing of thunderstorm-generated D-layer fluctuations by using time-domain lightning waveforms, *Geophys. Res. Lett.*, *38*, L23806, doi:10.1029/2011GL049790.

Lay, E. H., X.-M. Shao, and A. R. Jacobson (2014), *D* region electron profiles observed with substantial spatial and temporal change near thunderstorms, *J. Geophys. Res. Space Physics*, *119*, 4916–4928, doi:10.1002/2013JA019430.

Lefeuvre, F., J. L. Pinc¸on, and M. Parrot (2013), Midlatitude propagation of VLF to MF waves through nighttime ionosphere above powerful VLF transmitters, *J. Geophys. Res. Space Physics*, *118*, 1210–1219, doi:10.1002/jgra.50177.

Lin, Y. T., M. A. Uman, J. A. Tiller, R. D. Brantley, W. H. Beasley, E. P. Krider, and C. D. Weidman (1979), Characterization of lightning return stroke electric and magnetic fields from simultaneous two-station measurements, *J. Geophys. Res.*, *84*(C10), 6307–6314, doi:10.1029/JC084iC10p06307.

Mallick, S., V. A. Rakov, D. Tsalikis, A. Nag, C. Biagi, D. Hill, D. M. Jordan, M. A. Uman, and J. A. Cramer (2012), On remote measurements of lightning return stroke peak currents, *Atmos. Res.*, *135–136*, 306–313, doi:10.1016/j.atmosres.2012.08.008.

McDonald, T. B., III, M. A. Uman, J. A. Tiller, and W. H. Beasley (1979), Lightning location and lower-ionospheric height determination from two-station magnetic field measurements, *J. Geophys. Res.*, *84*(C4), 1727–1734, doi:10.1029/JC084iC04p01727.

McRae, W. M., and N. R. Thomson (2000), VLF phase and amplitude: Daytime ionospheric parameters, *J. Atmos. Sol. Terr. Phys.*, *62*(7), 609–618, doi:10.1016/S1364-6826(00)00027-4.

Ogawa, T., and T. Shimazaki (1975), Diurnal variations of odd nitrogen and ionic densities in the mesosphere and lower thermosphere: Simultaneous solution of the photochemical-diffusion equations, *J. Geophys. Res.*, *80*(28), 3945–3960, doi:10.1029/JA080i028p03945.

Pilkey, J. T. (2014), Rocket-triggered lightning propagation and north-florida thunderstorm charge structure, PhD dissertation, Univ. of Fla., Gainesville.

Pilkey, J. T., M. A. Uman, J. D. Hill, T. Ngin, W. R. Gamerota, D. M. Jordan, J. Caicedo, and B. Hare (2014), Rocket-triggered lightning propagation paths relative to preceding natural lightning activity and inferred cloud charge, *J. Geophys. Res. Atmos.*, *119*, 13,427–13,456, doi:10.1002/2014JD022139.

Rakov, V. A., and M. A. Uman (1990), Some properties of negative cloud-to-ground lightning flashes versus stroke order, *J. Geophys. Res.*, *95*(D5), 5447–5453, doi:10.1029/JD095iD05p05447.

Rakov, V. A., and M. A. Uman (2003), *Lightning Physics and Effects*, Cambridge Univ. Press, New York.

Rison, W., R. J. Thomas, P. R. Krehbiel, T. Hamlin, and J. Harlin (1999), A GPS-based three-dimensional lightning mapping system: Initial observations in central New Mexico, *Geophys. Res. Lett.*, *26*, 3573–3576, doi:10.1029/1999GL010856.

Schonland, B. F. J., J. S. Elder, D. B. Hodges, W. E. Phillips, and J. W. van Wyk (1940), The wave form of atmospherics at night, *Proc. R. Soc. London, Ser. A*, *176*, 180–202.

Shao, X.-M., and A. R. Jacobson (2009), Model simulation of very low-frequency and low-frequency lightning signal propagation over intermediate ranges, *IEEE Trans. Electromagn. Compat.*, *51*(3), 519–525, doi:10.1109/TEMC.2009.2022171.

Shao, X.-M., E. Lay, and A. R. Jacobson (2012), On the behavior of return stroke current and the remotely detected electric field change waveform, *J. Geophys. Res.*, *117*, D07105, doi:10.1029/2011JD017210.

Shao, X.-M., E. Lay, and A. R. Jacobson (2013), Reduction of electron density in the night-time lower ionosphere in response to a thunderstorm, *Nat. Geosci.*, *6*(1), 29–33, doi:10.1038/ngeo1668.

Smith, D. A., M. J. Heavner, A. R. Jacobson, X. M. Shao, R. S. Massey, R. J. Sheldon, and K. C. Wiens (2004), A method for determining intracloud lightning and ionospheric heights from VLF/LF electric field records, *Radio Sci.*, *39*, RS1010, doi:10.1029/2002RS002790.

Somu, V. B., V. A. Rakov, M. A. Haddad, and S. A. Cummer (2015), A study of changes in apparent ionospheric reflection height within individual lightning flashes, *J. Atmos. Sol. Terr. Phys.*, *136*, 66–79, doi:10.1016/j.jastp.2015.09.007.

Thomas, R. J., P. R. Krehbiel, W. Rison, S. J. Hunyady, W. P. Winn, T. Hamlin, and J. Harlin (2004), Accuracy of the Lightning Mapping Array, *J. Geophys. Res.*, *109*, D14207, doi:10.1029/2004JD004549.

Tonry, J., and M. Davis (1979), A survey of galaxy redshifts. I—Data reduction techniques, *Astron. J.*, *84*, 1511–1525, doi:10.1086/112569.

Uman, M. A., D. K. McLain, and E. P. Krider (1975),The electromagnetic radiation from a finite antenna, *Am. J. Phys.*, *43*, 33–38.

Uman, M. A., C. E. Swanberg, J. A. Tiller, Y. T. Lin, and E. P. Krider (1976), Effects of 200 km propagation on Florida lightning return stroke electric fields, *Radio Sci.*, *11*(12), 985–990, doi:10.1029/RS011i012p00985.

Wait, J. R., and K. P. Spies (1964), Characteristics of the Earth–ionosphere waveguide for VLF radio waves, NBS Tech. Note 300.

Walker, T. D. (2015), A 21st century investigation of the lightning spectrum, PhD dissertation, Univ. of Ala., Huntsville.

Weidman, C. D., and E. P. Krider (1980), Submicrosecond risetimes in lightning return-stroke fields, *Geophys. Res. Lett.*, *7*, 955–958, doi:10.1029/GL007i011p00955.

Westcott, B. S. (1962a), Ionospheric reflection processe for long radio-waves—I, *J. Atmos. Terr. Phys.*, *24*(5), 385–399.

Westcott, B. S. (1962b), Ionospheric reflection processe for long radio-waves—II, *J. Atmos. Terr. Phys.*, *24*(7), 619–631.

Willett, J. C., D. M. Le Vine, and V. P. Idone (2008), Lightning return stroke current waveforms aloft from measured field change, current, and channel geometry, *J. Geophys. Res.*, *113*, D07305, doi:10.1029/2006JD008116.